Test Report – Characterisation of concrete

1. Purpose and scope

This report presents the characterisation of hardened concrete according to the following parameters:

- Surface energy (measured by goniometry / contact angle),
- Pore diameter (size distribution),
- Surface roughness (3D profilometry),
- Effective porosity,
- Thermal conductivity,
- Density (apparent and skeletal).

The methods used, measurement uncertainty and standardised results are detailed.

2. Samples and preparation

The samples studied are cylindrical cores (test specimens) taken from concrete slabs 60 mm thick. The concrete is reinforced with internal steel reinforcement, which helps to limit or prevent the formation of cracks during handling of the blocks. The cores were extracted using a hole saw to produce cylinders 62 mm in diameter, without a central cavity. These test specimens therefore have a homogeneous geometry representative of the solid material, suitable for the various characterisation tests.

Prior to testing, all core samples were subjected to controlled drying at 40 °C in a ventilated oven for 4 days. The relative humidity of the ambient air in the laboratory (generally between 40 and 45 per cent) was maintained at a constant level. The test specimens were then left to stabilise for 3 days, until they reached a stable mass, defined as a relative variation of less than $\Delta m < 0.1$ per cent over 24 and 48 consecutive hours. It should be noted that no sanding, polishing or cleaning with solvents or water was carried out prior to the measurements. This procedure ensures a reproducible hygrometric state and minimises biases associated with residual moisture for all characterisation tests. The following table shows the correspondence between the concrete numbers and the names of the substrates used in the study.

Concrete 1	a1
Concrete 2	a2
Concrete 3	a3
Concrete 4	c
Concrete 5	b

3. Test methodologies

3.1. Apparent density

The apparent density (or bulk density) of hardened concrete is the ratio of the mass of the test specimen to its total apparent volume (solid + open/closed pores):

$$\rho_b = \frac{m}{V}.$$

The volume V is determined by hydrostatic weighing in accordance with standardised practices. As the test specimens are cores taken in situ, the hydrostatic method offers greater robustness than the geometric method when the faces are not perfectly parallel or plane-parallel, or when they have slight chips; it reduces the uncertainty in V and improves comparability between series. Its application involves considering:

$$\boldsymbol{V} = \frac{(\boldsymbol{m_{sss}} - \boldsymbol{m_i})}{\boldsymbol{\rho_{eau}}}$$

where$\boldsymbol{m_{sss}}$ is the saturated, wiped-dry mass,$\boldsymbol{m_i}$ the submerged mass, and$\boldsymbol{\rho_{eau}}$ the density of water in the thermostatic bath (at the specified temperature). From this, we deduce:

$$\rho_b = \rho_{eau} \cdot \frac{m_d}{m_{SSS} - m_i}$$

In operational terms, each test specimen is (after conditioning at 40 °C until its mass stabilises, see above): (i) saturated, (ii) wiped dry and then weighed to give$\boldsymbol{m_{sss}}$, (iii) weighed whilst submerged to give$\boldsymbol{m_i}$ (after removing any air bubbles), (iv) dried and weighed to give m_d. The above formulae are used to calculate$\boldsymbol{\rho_b}$ according to the reference state. For each mass state, five measurements (replicates) are carried out.

A check was carried out by weighing the sample twice, at +1 h and +2 h, under the same ambient conditions, in order to detect any possible deviations (residual evaporation, moisture reabsorption, buoyancy/bubbles). No deviations were observed.

3.2. Surface roughness by profilometry

Roughness was measured simply by profilometry on surfaces as taken (without sanding or polishing). For each core, representative areas were acquired within a fixed field of view (a few mm^2) with a micrometre-scale lateral step. The data were normalised and then filtered in accordance with ISO 25178, prior to the calculation of the Sa and Sq parameters. The results are presented as mean ± standard deviation (n areas per core) in order to provide an accurate picture of the actual condition of the surfaces for the interpretation of the measurements (wettability/adhesion, heat transfer).

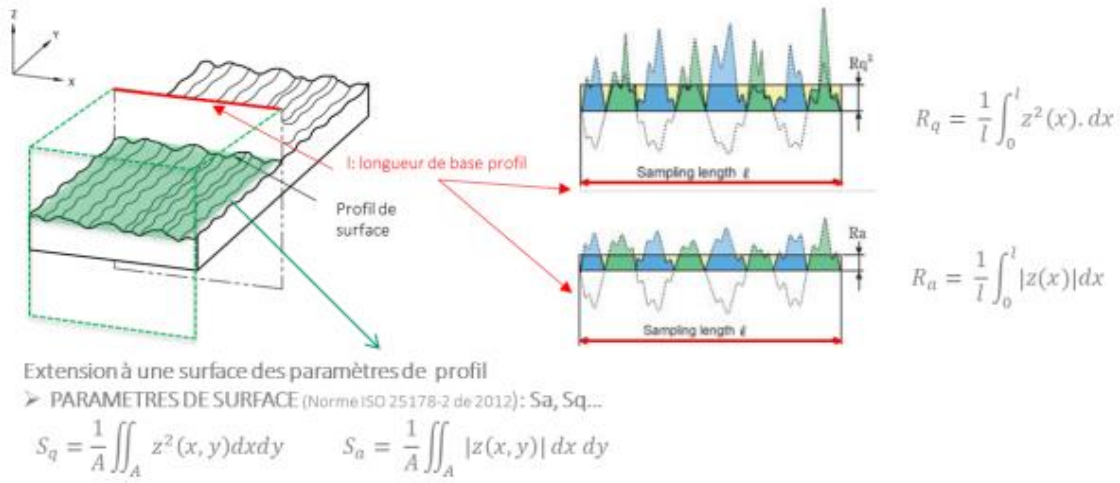


Figure1 . Schematic representation of the characterisation of surface parameters along a profile (Ra, Rq – standard NF EN ISO 4287) and across a surface (Sa, Sq – standard NF EN ISO 25178-2).

3.3. Pore size distribution (pore diameter)

The diameter of pores in concrete varies depending on the types of pores present, which influence its properties, particularly permeability and durability. These include, in particular:

- Air pores or entrained air bubbles, with diameters ranging from 10 µm to 1 mm.
- Capillary pores, generally with diameters between 0.01 µm and 5 µm. These pores are essential as they have the greatest influence on the permeability of concrete.
- Freeze pores, with diameters of less than 4 nm (40 Å), containing adsorbed water that is difficult to remove by drying.
- Macropores in the transition zone, with diameters between 0.1 and 1 µm.
- Effective air pores in air-entrained concrete, with diameters between 0.02 and 0.30 mm (20 to 300 µm), which provide protection against freezing.

Reducing the average diameter of capillary pores, particularly by lowering the water-to-cement ratio, decreases the porosity and permeability of concrete, thereby increasing its durability. Pore size and distribution therefore play a key role in the behaviour and resistance of concrete to external aggressions.

Depending on pore size, different measurement techniques can be used to determine the pore size distribution. Figure2 REF _Ref210914914 \h illustrates the two techniques employed in this study, namely:

- Gas adsorption porosimetry (N_2 at 77 K, Ar at 87 K, and possibly CO_2 at 273 K for ultra-micropores). This technique provides the specific surface area (BET) and the size distribution in the micro/mesoporous range (≈ 0.5–50 nm) via the analysis of adsorption/desorption isotherms.
- Mercury intrusion porosimetry (MIP). MIP primarily probes the pore throats of the network using the Washburn equation: $r = -2\gamma \cdot \cos\theta \ / P$ (where typically γ(Hg) ≈ 0.485 N·m^{-1} and θ ≈ 140° for cementitious matrices), which allows entry radii in the range of a few nanometres to a few hundred micrometres to be achieved, depending on the pressure (e.g. ≈ 3–5 nm at ~200–400 MPa).

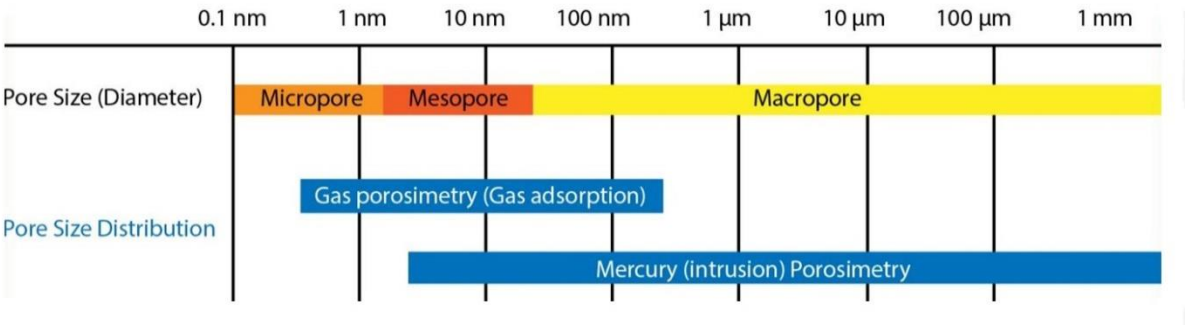


Figure2 . Techniques for measuring the pore distribution in concrete depending on the diameters to be characterised.

For the purposes of this study, only a MIP measurement was carried out.

3.4. Surface energy by goniometry (contact angle)

Principle: Goniometry is a method for assessing the surface properties of a material by measuring the contact angle formed by a drop of liquid on its surface (see Appendix). It is based on the equilibrium of surface tensions at the solid/liquid/vapour interfaces and enables the wettability of a solid and its surface energy to be determined.

The contact angle (static or dynamic) is defined as the angle formed at the triple interface between the solid, the liquid and the vapour. Its measurement is influenced by surface roughness and porosity, which can cause partial absorption of the liquid and alter the shape of the droplet (see Appendix).

The characterisation of surface energy properties was carried out according to the acid–base theory proposed by van Oss et al. This approach allows the surface energy to be decomposed into a Lifshitz–van der Waals-type dispersive component (γ^{LW}) and an acid–base polar component (γ^{AB}), which is itself split into acid (γ^{+}) and basic (γ^{-}) terms. Determining these components requires the measurement of contact angles with at least three liquids of different polarities. In accordance with the recommendations of Della Volpe et al. (2004) and Della Volpe & Siboni (1997, 2000), the selected triplet systematically comprises two polar liquids and one non-polar liquid in order to minimise the occurrence of negative values when calculating the components. For the purposes of this study, the liquids selected are: water, formamide and diiodomethane. Their surface energy properties are listed in the table below.

Table1 . Surface energy properties of the probe liquids.

Liquids	γ_L (mN/m)	γ_L^{LW} (mN/m)	γ_L^{AB} (mN/m)	γ_L^{+} (mN/m)	γ_L^{-} (mN/m)
Water	72.8	21.8	51.0	25.5	25.5
Formamide	58.0	39.0	19.0	2.28	39.6
Diiodomethane	50.8	50.8	0.0	0.0	0.0

Equipment: Contact angle measurements were carried out using an optical goniometer fitted with a microlitre drop deposition system and a high-resolution camera. The apparatus enables the precise deposition of drops of a few microlitres (water, formamide, diiodomethane) onto the surface of the samples. The behaviour of the droplet is recorded immediately after deposition and as the droplet grows through the addition of liquid (static and dynamic contact angles), under controlled lighting conditions, in order to minimise the effects of evaporation

and absorption by the porous substrate. Contact angles are determined by image analysis, using dedicated software that fits the droplet profile using the Young–Laplace equation.Figure3 shows the experimental goniometry setup used to measure contact angles, comprising the droplet deposition system, the imaging camera and the associated analysis software.

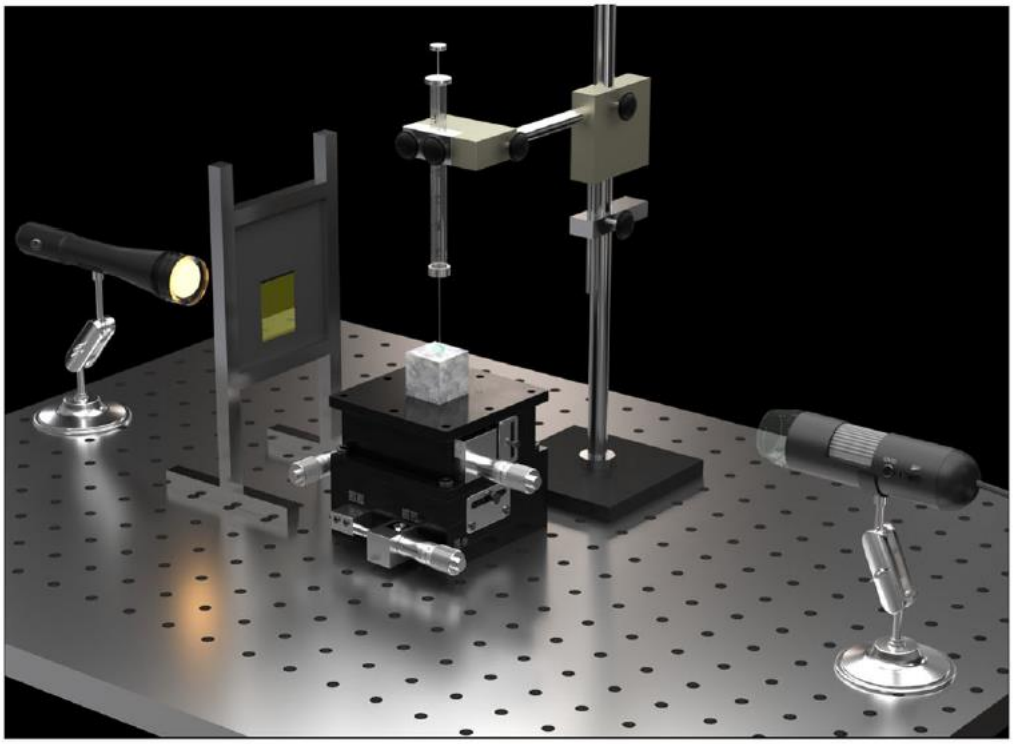


Figure3 . Illustration of a contact angle measurement setup [Kabir, 2023].

Methodology: The accuracy of contact angle (CA) measurements is influenced not only by the shape and volume of the droplets, but also by the fitting algorithm used to determine their profile. The following sections address these two aspects in turn in order to clarify the technical choices and implementations employed.

In order to rule out the effect of gravity, the droplet diameter must not exceed the capillary length (λ) of 2.73 mm for deionised water, estimated using the following equation:

$$\lambda = \sqrt{\frac{\gamma}{\rho \cdot g}}$$

where ρ is the density of the liquid (997 kg·m^{-3} for deionised water), g is the acceleration due to gravity (9.81 m·s^{-2}), and γ is the surface tension (≈ 71.99 mN·m^{-1} for deionised water; see the Methods section). Thus, the maximum volume of a drop of deionised water (at 23 °C and 50 % RH) must not exceed 10.7 µL to ensure that its geometry is not significantly distorted by its own weight. Conversely, droplets smaller than 3 µL should not be analysed as they are easily disturbed by the liquid dispensing system and by the prolonged dissipation of their kinetic energy. Furthermore, sub-microlitre-sized droplets (nano- and picolitres) can evaporate within

a few seconds (or even milliseconds) and require the use of very high-speed cameras (100–2000 fps).

In this study, the volume of the droplets used to characterise contact angles was determined using deionised water, with a target value of 4 ± 0.5 µL or 10 ± 0.5 µL, depending on the surfaces and the technical constraints encountered with those surfaces.

In-house software has been developed to accurately estimate contact angles from images and videos. The processing workflow is as follows: (i) importing images (raw format or video), (ii) selecting the region of interest (ROI) around the droplet (with automatic gradient-based cropping), (iii) detection of the baseline (solid–gas boundary) via robust regression, (iv) detection of the droplet contour via gradient analysis/segmentation, (v) sampling of at least N ≥ 6 points in the vicinity of each contact point, with a numerical step size $\Delta h \leq 0.05$, (vi) fitting the droplet profile using cubic *spline* polynomials and calculating the tangents at each triple point to obtain θ_{gauche} ,θ_{droite} andθ_{moyen} , (vii) metric calibration using the internal reference (fixed diameter of the injection syringe, measured separately using a precision tool). The parameters (N, Δh, ROI width, gradient thresholds) were optimised using a set of representative images in order to stabilise the estimation of the tangents against background noise and optical variations. The choice of *a* cubic *spline* limits the number of adjustments and reduces operator influence compared with the DropSnake method (ImageJ plugin[1]), whilst producing comparable measurements. In practice, the operator specifies the baseline and visually checks the fit of the contour; the rest of the processing is automated (pre- and post-processing, angle calculations, export). Validation was carried out on a common set of analysed images: (a) using the in-house software (cubic *spline*) and (b) using ImageJ/DropSnake. Comparability was assessed by (1) correlation of the measured contact angles, (2) mean bias and standard deviation, (3) paired agreement, and (4) sensitivity to operator settings (inter- and intra-operator repetitions). Both approaches yield consistent results, with the spline being simpler to implement (fewer parameters to adjust) and therefore less sensitive to the user's experience.

[1] ImageJ is a cross-platform, open-source image processing and analysis software package developed by the National Institutes of Health, http://imagej.nih.gov/ij/

3.5. Effective porosity

In this study, we focus on the effective porosity of different concretes, considering the concept of water-accessible porosity. This refers to the volume fraction of the test specimen consisting of open, interconnected pores into which water can actually penetrate.

$$\Phi_{eau} = \frac{V_{éprouvette}}{V_{eau\ absorbée}}$$

where $V_{éprouvette}$ and $V_{eau\ absorbée}$ represent the volumes of the concrete samples and the volume of water absorbed, respectively.

For operational purposes, this approach has been translated into a methodology using standard NF P 18-459, which allows Φ_{eau} to be estimated from three weighings: dry mass (m_d), saturated wiped mass (m_{sss}) and submerged mass (m_i) (hydrostatic weighing). The accessible porosity is then expressed as:

$$\Phi_{eau} = \frac{m_{sss} - m_d}{m_{sss} - m_i}$$

The term '$m_{sss} - m_i$' corresponds to the mass of water displaced and is given by $\rho_{eau} \cdot V$ (where ρ_{eau} is the density of water at the test temperature and V is the apparent volume).

The test was carried out in three identical cycles to verify stability and repeatability:

1. **Saturation:** immersion in water for 48 hours (covered bath, clean water, controlled temperature; degassed bath where possible to minimise bubbles).
2. **Weighing in the saturated state**:
    - remove the test specimen, wipe dry with a lint-free cloth; measure m_{sss} (balance accurate to 0.01 g);
    - weigh whilst submerged to obtain m_i ;
3. **Drying:** oven at 40 °C for 4 days, followed by stabilisation at constant mass (criterion: $\Delta m < 0.1\%$ over 24 h and 48 h), then measurement of m_d . A temperature of 40 °C is used to preserve the microstructure and avoid microcracking caused by 105 °C.

It should be noted that we carried out five weighings per condition (replicates) in order to estimate experimental variability, and we report only Φ_{eau} .

3.6. Thermal conductivity λ

Cf. Report.

4. Results

4.1. Apparent density and effective porosity

The apparent density and porosity were determined on the basis of 5 test specimens × 5 weighings (i.e. 25 values per concrete sample). The measurements and estimated values are recorded in theTable2 .

Table2 . Summary per concrete sample: 'dry' mass, apparent density, water absorptionA_w and effective porosityϕ_{eff} (mean ± expanded uncertainty (95%,$k = t_{0.975,\nu_{eff}}$ (Welch-Satterthwaite)). Note: pt = percentage point.

	'Dry' mass	Apparent density	A_w	Φ_{eff}
	g	$kg.m^{-3}$		
Concrete 1	973.04 ± 11.30	2304.7 ± 3.52	$4{,}05 \pm 0{,}50$ \%	9,25 % (±1,09 pt)
Concrete 2	991.51 ± 8.50	2285.2 ± 3.68	$3{,}90 \pm 0{,}27$ \%	8,78 %(±0,60 pt)
Concrete 3	988.61 ± 7.39	2340.8 ± 3.41	$3{,}77 \pm 0{,}22$ \%	8,76 %(±0,54 pt)
Concrete 4	953.43 ± 8.89	2178.6 ± 4.01	$5{,}45 \pm 0{,}19$ \%	11,89 %(±0,71 pt)
Concrete 5	993.64 ± 8.56	2,320.6 ± 3.13	$3{,}76 \pm 0{,}24$ \%	8,74 %(±0,57 pt)

With regard to 'dry' masses, the standard deviations reflect both inter-specimen variability (geometry, air content) and intra-specimen variability (repeatability of weighing). Individual intra-specimen deviations are generally very small, except in specific cases (e.g. specimen 4).

As regards bulk densities, the values are consistent with standard concrete (indicative range $\approx 2200 - 2400$ kg·m^{-3}), with the exception of concrete 4, which is lower ≈ 2182 kg·m^{-3}), which may indicate a higher air content consistent with its preparation. Two re-weighings were carried out at +1 h and +2 h (under the same ambient conditions) to verify the absence of drift (evaporation/re-wetting, buoyancy). No systematic changes were observed beyond the balance's resolution; the values used forρ_b are taken from the stabilised series. The uncertainties were calculated *using* the uncertainty propagation method (GUM) and the following formula:

$$u_c^2(\rho) = \left(\frac{\rho_w}{\Delta}\, u(m_d)\right)^2 + \left(\frac{m_d}{\Delta}\, u(\rho_w)\right)^2 + \left(\frac{\rho_w\, m_d}{\Delta^2}\, u(\Delta)\right)^2$$

where$u^2(\Delta) = u^2(m_{SSD}) + u^2(m_i)$.

As regards effective porosity (water-accessible),ϕ_{eff} is determined from the three weighings: dry massm_d , saturated mass on dry surfacem_{SSD} and submerged massm_i (hydrostatic weighing, at a controlled water temperature yieldingρ_w). The effective porosity is given by:

$$\phi_{eff} = \frac{m_{SSD} - m_d}{m_{SSD} - m_i} = \frac{V_{eau}}{V}$$

where$m_{SSD} - m_i = \rho_{eau} \cdot V$. The associated mass absorption is:

$$A_w(\%) = 100\, \frac{m_{SSD} - m_d}{m_d}$$

and the bulk densities are recalled for consistency:

$$\rho_{b,sec} = \rho_w \frac{m_d}{m_{SSD} - m_i}, \qquad \rho_{b,SSD} = \rho_w \frac{m_{SSD}}{m_{SSD} - m_i}.$$

The four concrete samples exhibit water absorption ratesA_w clustered around 3.8–4.1 per cent, consistent with effective porosities of ≈ 8.8–9.3 per cent based on the measured geometric volumes. The differences between the concrete samples remain modest; concrete sample 4, which appears slightly more porous, also has the lowest bulk density, which is consistent. The uncertainties were calculated *using* the uncertainty propagation method (GUM) and the following formulae:

$u_c^2(A_w) = \left(\frac{100}{m_d} \cdot u(\Delta)\right)^2 + \left(\frac{100 \cdot \Delta}{m_d^2} \cdot u(m_d)\right)^2$ (assuming thatΔ andm_d are independent), and,

$$u_c^2(\Phi) = \left(\frac{1}{\Gamma} \cdot u(m_d)\right)^2 + \left(\frac{\Gamma - \Delta}{\Gamma^2} \cdot u(m_{SSD})\right)^2 + \left(\frac{\Delta}{\Gamma^2} \cdot u(m_i)\right)^2$$

where$\Phi = \frac{\Delta}{\Gamma}$.

4.2. Pore size distribution

Figure4 shows the differential pore size distributions$dP_m/d\log r$ (cm^3/g) as a function of pore radius r (logarithmic scale, x-axis in Å). This quantity represents the volume intruded per unit decade of radius; the area under the curve is proportional to the intrudable porosity.

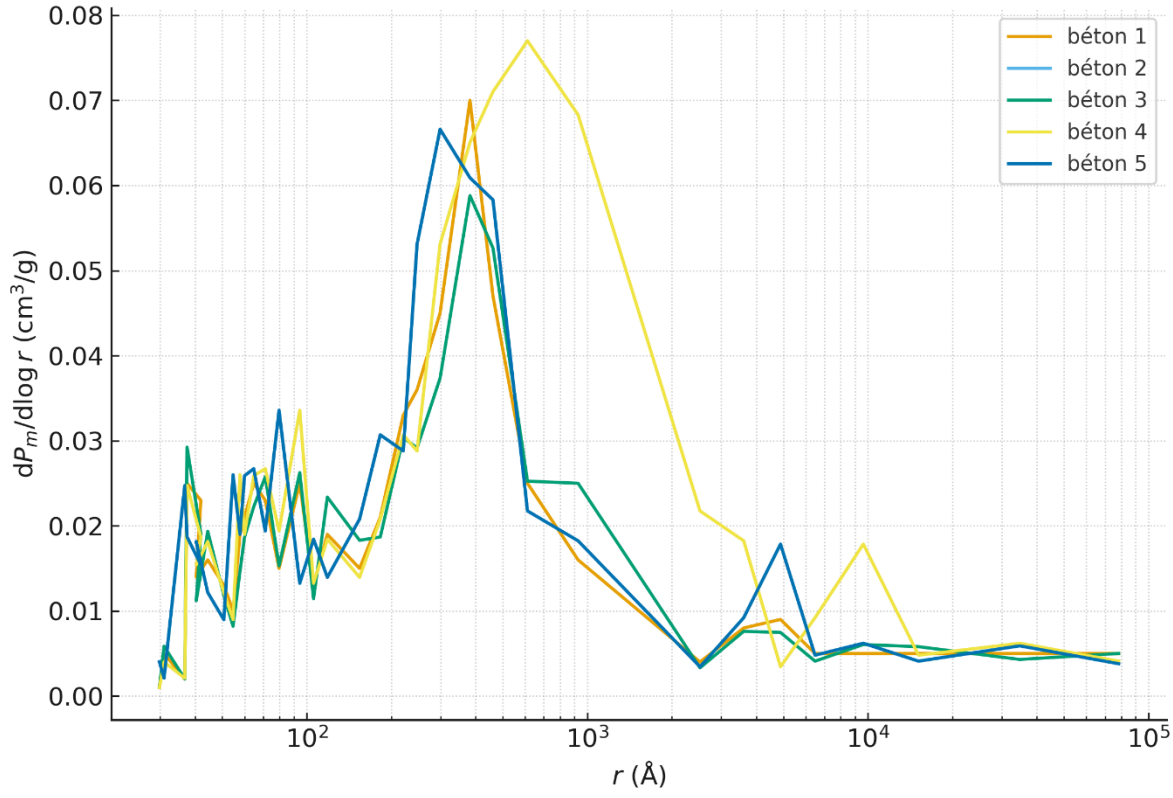


Figure4 . Differential pore size distribution,$dP_m/d\log r$ (cm^3/g)*, as a function of pore radiusr (logarithmic scale, Å) for five concrete specimens. Each curve corresponds to a concrete specimen (1 to 5). The area under*

the curve is proportional to the intrudable porosity and the peaks indicate the modal radii of the capillary network.

All five concrete samples exhibit a principal mode in the fine capillary range (approximately 30–100 nm). The following observations are made:

- Concrete 1: a maximum at around$r \approx 3{,}8 \times 10^2$ Å (~ 38 nm, amplitude ~0.07cm^3/g per decade), with a shoulder at around$3{,}8 \times 10^2$ Å .
- Concrete 2: two distinct peaks around 30–46 nm, amplitudes~0,06 – 0,067 cm^3/g .
- Concrete 3: peak centred at 38–46 nm, amplitude ~0.053–0.059.
- Concrete 4: coarser distribution: maximum around$6{,}1 \times 10^2$ Å (61 nm, ~0.077), very broad between 46–93 nm.
- Concrete 5: profile similar to Concrete 2 (dual mode ~30 and 40–46 nm).

Above 200 nm, the contributions become small for all samples, but it is noted that:

- Concrete 4 retains a significant contribution around 2.5–3.$^{6\times10^3}$Å, indicating a higher proportion of more open capillaries.
- Concretes 2 and 5 show a slight peak at ≈ 0.5 µm, greater than that of concretes 1 and 3.

The ascending order of capillary 'coarsening' (relative importance of radii >40–60 nm) is: Concrete 4 > Concrete 2 ≈ Concrete 5 > Concrete 3 ≈ Concrete 1.

This hierarchy is consistent with the other measured parameters: Concrete 4, which had the lowest bulk density and one of the highest effective porosities, shows here the greatest amplitude in the 60–100 nm range and a more pronounced tail, hallmarks of a more interconnected and potentially more permeable capillary network.

Concrete samples 2 and 5 are bimodal (peaks $\mathrm{at} \sim$ 30 nm and then ~ 40–46 nm), which may reflect a more spread-out capillary distribution (formulation/curing effect).

Concrete samples 1 and 3 remain finer, with maxima around 38–46 nm and low contributions above 0.2 µm, suggesting a less coarse capillary network.

4.3. Surface roughness

Roughness was characterised by profilometry and summarised using the following parameters: arithmetic roughnessS_a , mean square roughnessS_q . The values are reported as the mean ± standard deviation across three areas per concrete sample.

Table3 . Roughness parameters: arithmetic roughnessS_a and mean square roughnessS_q (in nm).

	Arithmetic roughnessS_a (nm)	Mean square roughnessS_q (nm)
Concrete 1	5394 ± 827	7043 ± 766
Concrete 2	6076 ± 489	7745 ± 495
Concrete 3	5735 ± 745	7498 ± 576
Concrete 4	4774 ± 258	6021 ± 428
Concrete 5	5967 ± 678	7658 ± 502

4.4. Surface energies.

Wettability measured by goniometry depends on the actual texture of the surfaces. When the geometric assumptions are met (droplets small enough to neglect gravity and ellipticity, and the base well contained within a locally homogeneous region), roughness corrections can be addressed within the framework proposed by Marmur (2003), based on the generalised Cassie–Baxter formulation. Within this framework, the apparent contact angle$\theta_{apparent}$ of a droplet on a rough/composite surface is related to the intrinsic Young's angle$\theta_{intrinsèque}$ (same chemistry, smooth surface) by:

$$\cos\theta_{apparent} = r_f \cdot f \cdot \cos\theta_{intrinsèque} + f - 1$$

where:

- r_f is the roughness factor of the wetted solid fraction (ratio of actual area to projected area over the regions actually in liquid–solid contact);
- f is the projected solid fraction actually in contact with the liquid (the complement,$1 - f$, representing the 'air' fraction beneath the drop);
- $\theta_{intrinsèque}$ is the intrinsic angle on a chemically identical smooth surface.

Roughness measurements are used to construct a digital surface that faithfully represents the topography, from which the following is derived:

- the local roughness factor$r_f(h)$ (actual area of wetted regions / projected area),
- the projected solid fraction$f(h)$ (projected area of wetted regions / total projected area), depending on a penetration parameter h for the liquid into the crevices. The couple$(r_f(h), f(h))$ used in the generalised Cassie–Baxter equation is evaluated at equilibrium$h = h_{eq}$ by minimising the Gibbs free energy of the system at the interfaces.

A simple and operational energy functional (per unit of projected areaA_{proj}) is:

$$G(h) = \gamma_{LV}\frac{S_{LV}(h)}{A_{proj}} + (\gamma_{SL} - \gamma_{SV})\frac{S_{SL}(h)}{A_{proj}}$$

whereγ_{LV} ,γ_{SL} ,γ_{SV} are the liquid–vapour, solid–liquid and solid–vapour interfacial tensions;$S_{LV}(h)$ and$S_{SL}(h)$ are the interfacial areas derived from the numerical surface area and the penetration depth h. The equilibrium state is defined by

$$\left.\frac{dG}{dh}\right|_{h=h_{!eq}} = 0, \qquad \left.\frac{d^{2G}}{dh^2}\right|_{h=h_{!eq}} > 0,$$

which givesh_{eq} , then$r_f = r_f(h_{eq})$ and$f = f(h_{eq})$. Substituting these into the previous equation yields the correction that relatesθapparent andθintrinsèque. . The plot (Figure5 , plot of$\cos\theta_{apparent}$ as a function of$\cos\theta_{intrinsèque}$) highlights the deviation due to texture and, conversely, allowsθintrinsèque to be identified from the corrected apparent measurements. In the case of the concretes analysed here, the deviation is truly minimal.

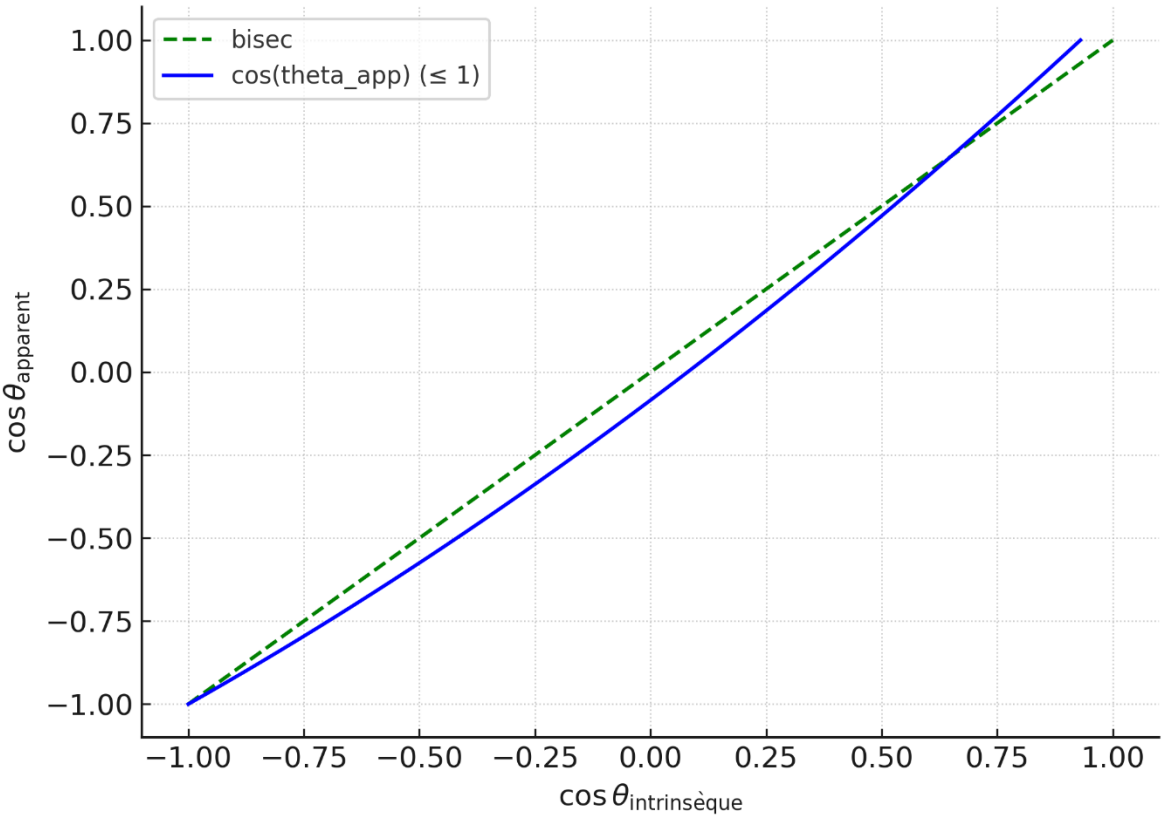


Figure5 . Illustration of a plot of $\cos\theta_{\text{apparent}}$ *as a function of* $\cos\theta_{\text{intrinsèque}}$ *for the open-ended specimen a1, considering water as the probe liquid.*

Table4 . Measurements of the corrected contact angles for the three probe liquids.

	Diiodomethane	Formamide	Water
Concrete 1	23 ± 3	19 ± 2	11 ± 1
Concrete 2	21 ± 2	18 ± 3	11 ± 2
Concrete 3	21 ± 3	19 ± 1	10 ± 1
Concrete 4	19 ± 4	15 ± 2	11 ± 2
Concrete 5	22 ± 4	15 ± 4	11 ± 2

According to the van Oss–Chaudhury–Good (vOCG) theory and the contact angle values from theTable3 , it is possible to estimate the dispersiveγ_S^{LW} , , acidicγ_S^+ , basicγ_S^- , acid–base$\gamma_S^{AB} = 2\sqrt{\gamma_S^+\gamma_S^-}$, and totalγ_S components at the interface. For information, the uncertainties associated with the surface energy components were evaluated using Monte Carlo simulation (10^5 draws), by jointly propagating the uncertainties in the contact angles and the liquid constants (normal, independent laws) and reporting the median as the estimator with the 95% coverage interval ($k \approx 2$), in accordance with the GUM.

Table5 . Estimation of surface energy components for different concretes.

	γ_S^{LW} $(mN \cdot m^{-1})$	γ_S^+ $(mN \cdot m^{-1})$	γ_S^- $(mN \cdot m^{-1})$	γ_S^{AB} $(mN \cdot m^{-1})$	γ_S $(mN \cdot m^{-1})$
Concrete 1	46.84 ± 5.23	0.12 ± 0.1	57.88 ± 3.87	5.3 ± 0.54	52.14 ± 7.34
Concrete 2	47.48 ± 4.23	0.11 ± 0.07	57.43 ± 5.43	5.07 ± 0.1	52.55 ± 5.41
Concrete 3	47.48 ± 3.33	0.09 ± 0.03	58.4 ± 5.81	4.49 ± 0.74	51.97 ± 7.1
Concrete 4	48.07 ± 5.43	0.15 ± 0.04	56.13 ± 5.1	5.72 ± 0.48	53.79 ± 8.3
Concrete 5	47.17 ± 4.64	0.2 ± 0.1	56.04 ± 5.97	6.7 ± 0.64	53.87 ± 5.34

The total surface energies range from$52 \text{ et } 54 \text{ mN} \cdot \text{m}^{-1}$, , dominated by a dispersive component (~47–48$\text{mN} \cdot \text{m}^{-1}$) and a more moderate acid–base component (~4.5–6.7$\text{mN} \cdot \text{m}^{-1}$). All surfaces are strongly basic ($\gamma_S^- \gg \gamma_S^+$), consistent with the chemistry of cement hydrates. The 'γ_S' classification is B5 ≥ B4 > B2 ≥ B1 > B3, with B5 characterised by the strongest polar interaction.

4.5. Summary table

To conclude the characterisation, we have compiled the key indicators for each concrete—apparent density, surface roughness (ISO 25178 parameters:S_a, S_q), and surface energies obtained using the van Oss–Chaudhury–Good model based on contact angles (water, formamide, diiodomethane)—in the table atTable6 . The uncertainties in the energies were evaluated using Monte Carlo simulation (joint propagation of contact angles and liquid constants), and the densities are accompanied by their expanded uncertainty (k≈2).

Overall, the five concretes exhibit high total energies (~$52 - 54 \text{ mN} \cdot \text{m}^{-1}$) dominated by the dispersive componentγ_S^{LW} (~$47 - 48 \text{ mN} \cdot \text{m}^{-1}$),) with a moderate acid–base contribution (~4.5–

$6.7\mathrm{mN}\cdot\mathrm{m}^{-1}$),) reflecting highly basic surfaces($\gamma_S^- \gg \gamma_S^+$) — consistent with the low angles measured. In terms of texture, Concrete 2 is the roughest (S_a, S_q s are higher), whilst Concrete 4 is the smoothest (and also has the lowest bulk density). We would therefore expect, on hydrophilic surfaces , lower apparent contact angles and more pronounced hysteresis for the roughest concretes, whilst the smoothest concrete exhibits more stable contact angles. Finally, Concrete 5 is characterised by the strongest polar component(γ_S^{AB}), indicating a more pronounced interaction with polar liquids.

Table6 . Summary by concrete type: bulk density, roughnessS_a/S_q and surface energies(γ_S^{LW}, γ_S^{AB}, γ_S). Values are given as mean ± SE (or 95% CI where specified).

Concrete	Apparent density ($kg\cdot m^{-3}$)	S_a (nm)	S_q (nm)	γ_S^{LW} ($mN\cdot m^{-1}$)	γ_S^{AB} ($mN\cdot m^{-1}$)	γ_S ($mN\cdot m^{-1}$)
1	2304.7 ± 3.52	5394 ± 827	7043 ± 766	46.84 ± 5.23	5.30 ± 0.54	52.14 ± 7.34
2	2285.2 ± 3.68	6076 ± 489	7745 ± 495	47.48 ± 4.23	5.07 ± 0.10	52.55 ± 5.41
3	2340.8 ± 3.41	5735 ± 745	7498 ± 576	47.48 ± 3.33	4.49 ± 0.74	51.97 ± 7.10
4	2181.6 ± 3.59	4774 ± 258	6021 ± 428	48.07 ± 5.43	5.72 ± 0.48	53.79 ± 8.30
5	2320.6 ± 3.13	5967 ± 678	7658 ± 502	47.17 ± 4.64	6.70 ± 0.64	53.87 ± 5.34

Appendix A – Wettability

Wetting of perfect surfaces

The surface free energies of solids cannot be measured directly. Various independent approaches are therefore used to estimate them, including, in particular, wettability measurements. These involve depositing a drop of liquid with known surface tension onto a solid. Due to the specific interactions occurring at the interface between the solid, the liquid and its vapour, the drop adopts a spatial configuration which, at thermodynamic equilibrium, corresponds to the minimum energy of the system. Measurements carried out for different liquids can then be used to determine the surface energy components of the solid.

To address the case of partial wetting, as early as 1805 Young considered a system consisting of a flat, non-deformable, smooth, chemically homogeneous solid substrate that was partially wetted by a liquid. He proposed a vector representation of the forces acting on the shape of the dropFigure6).

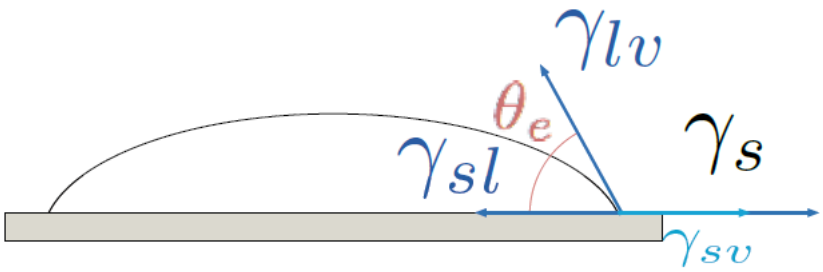


Figure6 . Diagram of a water droplet partially wetting a solid surface. The contact angle

By considering the energy associated with the system shown inFigure6 for an infinitesimal displacement of the contact line, Young's work led him to establish that, at thermodynamic equilibrium, surface tensions are related to one another by the following equation:

$$\gamma_{SV} = \gamma_{SL} + \gamma_{LV} \cos\theta$$

whereγ_{LV} ,γ_{SV} andγ_{SV} are, respectively, the surface tensions at the liquid–vapour, solid–vapour and solid–liquid interfaces.

The above equation therefore establishes a link between the surface energies of the solid surfaces under investigation (γ_{SV}), the energetic properties of the liquid (γ_{LV}) used for the measurement, and the surface energies arising from the liquid–solid surface interaction. This unique link for any liquid–surface pair is fully quantified by the value of the angle μ, which is the subject of wettability measurements.

Determining the surface energies of ideal surfaces

Ultimately, Young's equation contains the experimentally determined parameters γ_{LV} and $\cos\theta$, and relates them to the surface energy of the solid phase of interest γ_{SV}. One unknown remains, however: the solid–liquid interfacial energy γ_{SL}.

In order to evaluate the γ_{SV} component using Young's equation, various theories describe γ_{SL} as a function of γ_{SV} and specific interactions between the solid and the liquid [Sharma and Rao, 2002]. The first models of γ_{SL} proposed and presented in the literature involve expressing γ_{SL} in terms of solid and liquid surface energies via an equation of state [Kwok and Neumann, 2000]. A second approach empirically approximates the solid surface energy by introducing the concept of the critical angle, corresponding to the surface tension that separates fully wettable and partially wettable liquids on the solid in question [Fox and Zisman, 1952]. Finally, the Acid-Base theory involves decomposing the total surface energy in order to express the solid-liquid interfacial energy γ_{SL}.) in terms of solid and liquid surface energies [Owens and Wendt, 1969; Van Oss et al., 1986; Fowkes, 1987].

Only this approach is discussed here, as it attempts to explain the origin of surface energies through van der Waals and Lewis acid-base interactions.

The Acid-Base Theory The model known as the 'Acid-Base Theory' stems from the work initiated by Fowkes [1987]. It posits that the physical interactions between bodies in contact result from a combination of contributions of various kinds, as mentioned previously. Over the following decades, Van Oss, Chaudhury and Good (VCG) expanded on this approach, ultimately concluding that:

$$\gamma_{LV}(1+\cos\theta) = 2\left(\sqrt{\gamma_{SV}^{LW}\gamma_{LV}^{LW}} + \sqrt{\gamma_{SV}^{+}\gamma_{LV}^{-}} + \sqrt{\gamma_{SV}^{-}\gamma_{LV}^{+}}\right)$$

where, for a {liquid–surface} pair, the following are taken into account:

- θ, the contact angle of the droplet deposited on the surface;
- γ_{LV}^{LW}, γ_{LV}^{-}, γ_{LV}^{+} : the energy components of the liquid used;
- γ_{SV}^{LW}, γ_{SV}^{-}, γ_{SV}^{+} : the energy components of the solid to be characterised.

Since the aim of wettability studies is to evaluate the surface energy of the solid, the above equation suggests that determining the contact angles associated with three different liquids is sufficient to calculate γ_{SV}.

When chosen appropriately, the liquids commonly considered are two polar liquids and one non-polar liquid.

Methods for measuring wettability

For solid samples, contact angles can be measured in two ways: either in static mode or in dynamic mode.

In static mode, the profile of a stationary droplet deposited on a substrate is studied

using a camera and image processing software. The angle measured is simply that of the drop resting on the surface and is the angle most frequently cited in the literature.

In dynamic mode, the focus is on the phenomenon known as contact angle hysteresis. Owing to surface roughness and/or inhomogeneities, this hysteresis corresponds experimentally to the difference observed between the measured apparent contact angle and the angle that would have been measured on the corresponding ideal surface. Thus, to minimise the variation associated with static angle measurements, the advancing angle is generally used for surfaces that are sufficiently smooth and homogeneous [Neumann et al., 1974]. The advancing angle μa corresponds to the contact angle measured at the moment the triple line begins to move (Figure 1.4). It is obtained by adding liquid to a drop previously formed on a surface or by tilting the substrate on which the drop is deposited, and then recording the angle at which the triple line begins to move.

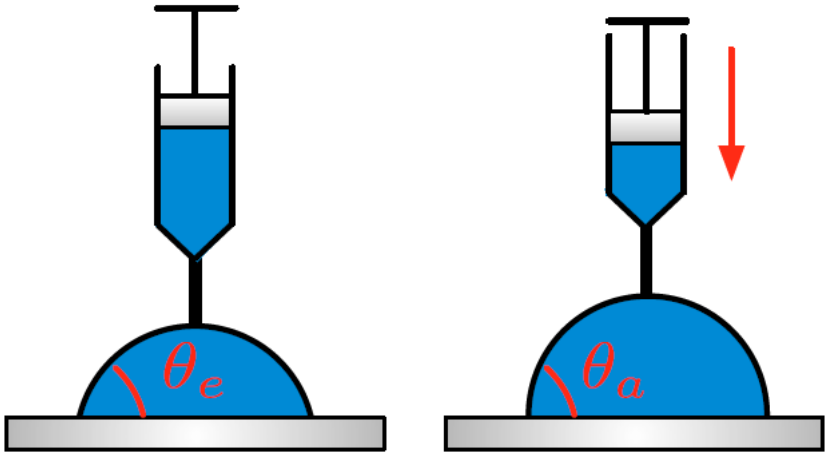


Figure7 . Illustration of a measurement of the advance angle of a liquid on a surface.

Wetting of textured surfaces

As Johnson and Dettre observed, water droplets placed on a rough hydrophobic substrate can exhibit very different behaviours depending on the surface roughness [Dettre and Johnson, 1964]. This observation, subsequently confirmed by other, more modern experiments, raises the question of surface roughness and its inclusion in surface wettability models, which remains essential. Two possible wetting scenarios, known as the Wenzel and Cassie-Baxter scenarios (Figure 1.5), are highlighted.

The Wenzel model: Wenzel was the first, in 1936, to investigate the dependence of the contact angle on roughness. He sought to define the apparent contact angleθ^* on a rough surface as a function ofθ_{eq} and the surface roughness r [Wenzel, 1936]. This dimensionless term r is defined as the ratio of the effective surface area (taking account of surface asperities) to the corresponding geometric plane surface area, and is therefore a number greater than or equal to 1.

Assuming that Young's law holds locally, Wenzel's model establishes that:

$$\cos\theta^* = r \cdot \cos\theta_{eq}$$

The Cassie–Baxter model In 1944, Cassie and Baxter introduced a concept known as 'air pockets', whereby, in order to describe the wettability of porous surfaces, the crevices in the substrate trap small pockets of air between the liquid and the substrate [Cassie and Baxter, 1944]. Cassie generalised this description in 1948, extending his analysis to chemically heterogeneous surfaces. His reasoning, based on an energy-based description similar to that proposed by Wenzel, allows us to consider a drop resting on a smooth surface composed of n types of materials randomly distributed across the flat substrate. Each material is characterised by its own coefficients °i,sl and °i,sv, as well as by the fraction fi of the substrate surface with $f_1 + \cdots + f_n = 1$.

The formulation giving the apparent Cassie-Baxter contact angle then involves

to averaging the cosines of the angles on each of the n surfaces, weighting each term by the corresponding surface fractions:

$$\cos\theta^* = \sum_{i=1}^{n} f_i \cos\theta_{eq,i}$$

where i denotes the surfaces considered for the measurement of contact angles.

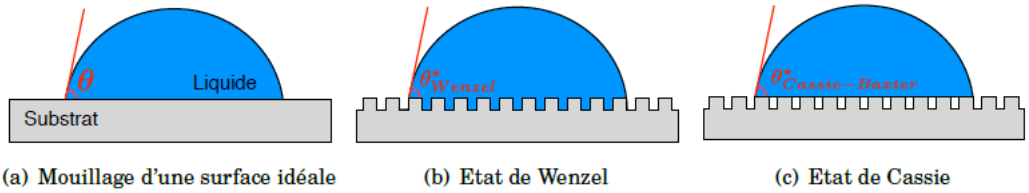


Figure8 . Illustration of the three possible states of wetting of a surface: partial wetting of an ideal surface (a), wetting by a liquid conforming to the solid surface (b) and wetting by a liquid resting on the peaks of the asperities (c).

Reconciliation of the Wenzel and Cassie-Baxter models The need to understand the dynamic processes of wetting has led to the more precise development of the underlying wetting models. However, proposing a formulation to describe the equilibrium state of a drop resting on a hydrophobic surface proves to be a challenging problem. This is evidenced by the plethora of (often erroneous) rewritings and reinterpretations of the Wenzel and Cassie-Baxter equations [Milne and Amirfazli, 2012]. Among the established findings, various studies highlight the investigation of variations in the Gibbs energy function [Wolansky and Marmur, 1998; Brandon et al., 2003; Marmur, 2003; Marmur and Bittoun, 2009]. By assuming that a deposited drop is large compared to the wavelength of the surface irregularities or chemical inhomogeneities, the approximation remains valid and places the Wenzel and Cassie-Baxter equations within a well-defined mathematical and thermodynamic framework.

The necessary conditions for the transition between regimes of homogeneous and heterogeneous wettability are then derived from the determination of the local extrema of the Gibbs function with respect to the apparent contact angle μ? and the fraction of wetted solid,

f. For cases of partial wetting , the conclusions of the study of variations lead to a formulation of the Cassie-Baxter relationship:

$\cos\theta^{*} = r_f \cdot f \cdot \cos\theta + f - 1.$

Bibliography

ABD Cassie and S Baxter. Wettability of porous surfaces. Transactions of the Faraday Society, 1944.

C. Della Volpe and S. Siboni. Some reflections on acid–base solid surface free energy theories. Journal of Colloid and Interface Science, 1997.

C Della Volpe and S Siboni. Acid–base surface free energies of solids and the definition of scales in the Good–van Oss–Chaudhury theory. Journal of Adhesion Science and . . . , 2000.

C Della Volpe, D Maniglio, M Brugnara, and S Siboni. The solid surface free energy calculation: I. In defence of the multicomponent approach. Journal of Colloid and . . ., 2004.

Marmur, A. (2003). Wetting on hydrophobic rough surfaces: to be heterogeneous or not to be?. *Langmuir*, 1920), 8343–8348.

Abraham Marmur and Eyal Bittoun. When Wenzel and Cassie are right: reconciling local and global considerations. Langmuir, 253): 1277–1281, 2009.

A W Neumann, R J Good, C J Hope, and M Sejpal. An equation-of-state approach to determine surface tensions of low-energy solids from contact angles. Journal of Colloid and Interface Science, 492: 291–304, November 1974.

D K Owens and R C Wendt. Estimation of the surface free energy of polymers. Journal of Applied Polymer Science, 1969.

L H Sharpe and H Schonhorn. Surface Energetics, Adhesion, and Adhesive Joints. In pubs.acs.org, pp. 189–201. AMERICAN CHEMICAL SOCIETY, WASHINGTON, D.C., January 1964.

C J Van Oss, R J Good, and M K Chaudhury. The role of van der Waals forces and hydrogen bonds in "hydrophobic interactions" between biopolymers and low-energy surfaces. Journal of Colloid and Interface Science, 1112): 378–390, June 1986.

Gershon Wolansky and Abraham Marmur. The Actual Contact Angle on a Heterogeneous Rough Surface in Three Dimensions. Langmuir, 14(18):5292–5297, September 1998.